forum acusticum 2026
8-12 September · Graz, Austria

EXPERIMENTAL ANALYSIS OF LEADING-EDGE DIFFRACTION FROM FINITE-SIZED RIGID AND POROUS PLATES UNDER GRAZING INCIDENCE

Arif Onur Yürek, Aleksi Öyry, Tapio Lokki

Acoustics Lab, Department of Information and Communications Engineering, Aalto University, Finland

This paper is a revised version of the authors' submitted manuscript that was peer-reviewed by at least two anonymous reviewers.

Abstract

Leading-edge diffraction and early scattering from finite-sized rigid, porous, and perforated plates under grazing incidence are investigated using measurements acquired on a dense planar grid with a moving-microphone. A signal-subtraction approach is employed to isolate sample-induced contributions followed by arrival-time-locked, band-adaptive time-windowing. The resulting edge-induced level distributions are analysed across multiple grazing angles. A rigid plate serves as a reference condition, enabling consistent characterization of the measured fields. The responses of porous and perforated samples are evaluated both independently and relative to this reference, allowing systematic identification of material-dependent modifications in the early diffraction field. The proposed approach provides a systematic framework for assessing edge-dominated scattering from finite-sized samples under grazing-incidence conditions.

Keywords: *diffraction, porous absorbers, finite size, grazing incidence, field separation*

1. Introduction

Sound interaction with boundaries governs reflection, diffraction, scattering, and absorption, and becomes particularly complex near finite-sized objects where multiple wave phenomena coexist. This complexity is further amplified under shallow grazing incidence, where incident, diffracted, and scattered contributions strongly overlap in both space and time, making experimental separation and physical interpretation challenging.

While edge diffraction has been extensively studied for canonical rigid geometries, primarily based on idealized configurations such as infinite wedges and baffled edges [1], [2], [3], most investigations rely on simplified assumptions. In practical applications, however, acoustic treatments often consist of finite-sized and porous materials, for which edge-related effects can significantly influence the local sound field. Deviations from idealized edge behaviour have been reported for finite and more complex geometries [4], where multiple interactions and thickness effects become relevant. Similarly, diffraction at impedance edges has been shown to involve modified radiation characteristics compared to rigid edges, leading to a redistribution of diffraction energy in space [5], [6], [7]. Recently, these effects were incorporated into generalized edge-diffraction formulations for impedance surfaces [8].

Under grazing incidence, the incident, diffracted, and scattered components become increasingly coupled in both space and time, significantly complicating their experimental separation. Existing sound-field separation methods become increasingly difficult to apply under grazing incidence because of the strong overlap of incident, reflected, and diffracted wave components, particularly for finite absorbers [9]. These limitations motivate measurement-based approaches that directly isolate the scattered field from measured impulse responses.

In the present work, dense planar measurements of impulse responses are acquired near finite-sized rigid, porous, and perforated samples under grazing incidence. Over the analysed region, the incident wavefront is approximated as locally planar. The analysis is restricted to a sub-grid located near the leading edge, where the influence of specular reflection is minimized and the measured field is therefore assumed to be diffraction dominated. A signal subtraction approach, originally proposed in [10] and further developed in [11], is employed to subtract corresponding free-field reference measurements, thereby suppressing the direct-field contribution. Subsequently, a diffraction-locked, band-adaptive time-windowing procedure is applied to analyse the transient diffraction response, in which the analysis window is aligned with

Corresponding author: *arif.yurek@aalto.fi.*

the local diffraction arrival and its duration is adapted to the analysed frequency band. The resulting responses are represented in terms of diffraction-induced level relative to a rigid reference, allowing material-dependent changes within the diffraction-dominated region to be quantified.

2. Experiments

The tested samples had varying thicknesses and included a rigid plate (2 cm), a perforated gypsum board (1 cm), a perforated glass-wool panel (4 cm), and a bioboard (foam-formed cellulose) porous absorber (3 cm). All samples had surface dimensions of 68×68 cm, except for the glass wool, which measured 50×50 cm. To ensure a common diffraction geometry, its leading edge was aligned with those of the other materials. All samples were measured individually, while the bioboard panel was additionally measured with the rigid backing. Fig. 1a shows the tested materials.

The test sample and motorized mover were mounted on a rigid frame designed to provide precise and repeatable positioning. A directional loudspeaker (Panphonics, Finland) approximating a plane-wave source (60×60 cm aperture) was used for sound field excitation. The source was mounted on a horizontal beam, allowing lateral translation to realize different incidence angles. The sample was mounted vertically on a cantilevered support using a compact two-part clamping holder. This arrangement enabled repetitive scanning of an identical aperture while maintaining a fixed surface plane, independent of sample thickness. A lateral view of the setup is shown in Fig. 1b.

A planar aperture perpendicular to the material surface was scanned using a single microphone driven by a motorized mover system. At each position, a time-domain impulse response (IR) was acquired. Repeating this procedure over the full grid yielded a spatially sampled pressure field equivalent to a planar microphone array. Measurements were conducted both in the free field and in the presence of the test samples using identical source–receiver geometry.

For visualization, the measured geometry is expressed in a presentation-oriented Cartesian coordinate system in which the scanning aperture lies in the x–z plane ($y = 0$) and the sample surface corresponds to $z = 0$, while preserving the relative spatial arrangement of source, sample, and receiver positions.

The global scanning aperture consisted of 72×31 measurement positions, with a spatial resolution of 1 cm along the surface-parallel (x) direction. Along the surface-normal direction, the step size was 1 cm near the sample and increased to 3 cm at larger distances, with the closest measurement line located 1 cm from the surface. In the current paper, the analysis is restricted to a sub-array of 21×21 positions in front of the leading edge to minimize the influence of specular reflections while maintaining a uniform 1 cm microphone spacing in both x and z directions.

The grazing angle of incidence was defined as the angle between the sample surface ($z = 0$) and the line connecting the acoustic center of the source to the center of the sample, defined in the x–z plane (see Fig. 1c). Measurements were conducted at nominal grazing angles of 0°, 5°, 8°, 11°, 20°, and 30°, while perforated samples were measured only at 8° and 30°.

Prior to each measurement, the sample orientation was verified using laser levels and by traversing the microphone along the first row near the surface. The excitation signal was a sine sweep spanning 100 Hz– 20 kHz. Each signal consisted of 1 s silence, a 3 s sweep, and a final 1 s silence to allow mechanical vibrations to decay. Additional pauses were introduced between positions to ensure scanner settling.

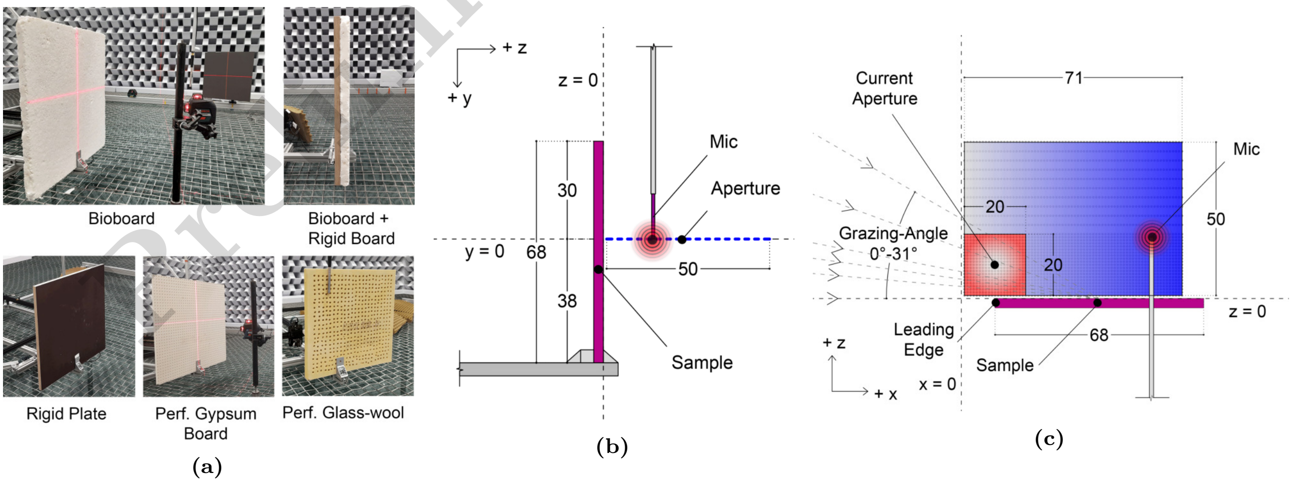

Figure 1: (a) Measured samples: bioboard ($68 \times 68 \times 3$ cm), rigid plate + bioboard ($68 \times 68 \times 5$ cm), perforated glass wool ($50 \times 50 \times 4$ cm), rigid plate ($68 \times 68 \times 2$ cm), and perforated gypsum board ($68 \times 68 \times 1$ cm). The planar source used for excitation is visible in the top-left panel. (b) Lateral view of the setup. The orientation corresponds to the measurement configuration. (c) Top view of the installed sample (68×68 cm), showing the microphone positions, scanned aperture and the grazing angles of incident sound (units in cm). The propagation directions are shown with arrows.

3. Post-Processing

In this paper, receiver positions are described by their physical coordinates (x, z) within the aperture plane $y = 0$. The discretized grid corresponds to uniformly spaced positions along the surface-parallel (x) and vertical (z) directions.

3.1. Estimation of Effective Incidence Angle

The effective grazing angle was estimated from the free-field measurements to compensate for small geometric deviations from the nominal setup. For grazing angles between 5° and 30°, the propagation direction was obtained from the mean phase gradients of the free-field wave field over a subset of receivers ($x = 1{:}20$, $z = 1{:}20$) using frequencies between 2 and 6 kHz, while the 0° case was estimated from a linear regression of the free-field arrival time. The resulting effective grazing angles were rounded to the nearest integer, yielding 0°, 5°, 8°, 11°, 21°, and 31°, and were subsequently used to define the effective source geometry for the analysis.

3.2. Time-Alignment, Calibration and Subtraction of Signals

To isolate the sample-induced contributions in the measured sound field, the surface measurements were first time-aligned and amplitude-calibrated with respect to the corresponding free-field measurements. Small relative delays and amplitude mismatches between the two measurement sets may arise from slight variations in the effective sound speed and other geometric uncertainties associated with separate moving-microphone measurement realizations.

At receiver positions close to the sample surface, early scattered arrivals may bias both the delay and amplitude estimates. These positions were identified using a statistical procedure, and the corresponding correction factors were estimated from neighbouring receiver positions within the same measurement column. The resulting delay and amplitude corrections were subsequently used throughout the alignment and calibration procedures.

For each receiver position (x, z), the relative delay between the surface response $p^{\mathrm{sur}}(t, x, z)$ and the free-field response $p^{\mathrm{ff}}(t, x, z)$ was estimated by cross-correlation within a time window centred on the free-field incident peak. Sub-sample accuracy was achieved by exponential interpolation of the cross-correlation peak, yielding the delay estimate $\tau(x, z)$ expressed in original sampling intervals.

Delay compensation was performed in the frequency domain. Let $P^{\mathrm{sur}}(f, x, z)$ denote the discrete Fourier transform of $p^{\mathrm{sur}}(t, x, z)$. The aligned spectrum is obtained via linear phase correction,

$$P^{\mathrm{sur,aligned}}(f, x, z) = P^{\mathrm{sur}}(f, x, z)\, e^{-j2\pi f \tau(x,z)}. \quad (1)$$

Residual amplitude mismatches were corrected per receiver column. For each column x, a calibration factor $b(x)$ was obtained from the ratio between the root-mean-square (RMS) amplitudes of the aligned surface and free-field signals, i.e., $p_{\mathrm{sur,aligned}}(t, x, z)$ and $p_{\mathrm{ff}}(t, x, z)$. The RMS values were evaluated over short Tukey-windowed segments centered on the incident peak.

The calibrated surface response is defined as

$$p_{\mathrm{sur,cal}}(t, x, z) = b(x)\, p_{\mathrm{sur,aligned}}(t, x, z). \quad (2)$$

The indirect-field response is then obtained by subtracting the free-field response:

$$p_{\mathrm{ind}}(t, x, z) = p_{\mathrm{sur,cal}}(t, x, z) - p_{\mathrm{ff}}(t, x, z). \quad (3)$$

Next, all indirect-field responses were deconvolved using an angle-specific free-field reference measurement recorded at a designated receiver at the centre of the analysed sub-grid ($x = 11$, $z = 11$). A regularized cross-spectral frequency-domain deconvolution with spectral smoothing was applied to suppress the source signature and improve the temporal localisation of the scattered-field response. A causal fade based on the rigid case was then applied to suppress pre-arrival subtraction residuals. A sensitivity analysis confirmed that the causal fade had a negligible influence on the extracted band amplitudes above 315 Hz. Figure 2 illustrates the event-locked windowing procedure for the 630 Hz band applied to the processed indirect-field IRs obtained at microphone position $x = 6$, $z = 6$ and a grazing angle of 31°.

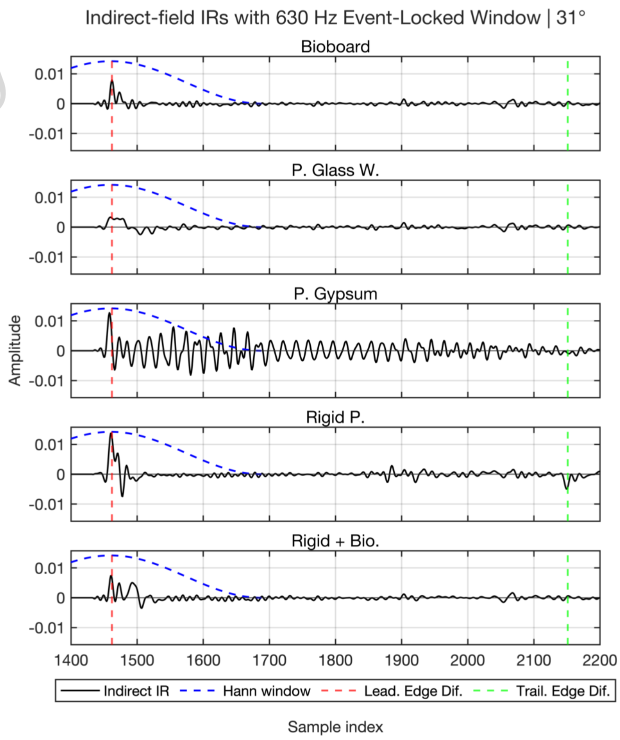

Figure 2: Processed scattered-field IRs obtained above all materials at microphone position $x = 6, z = 6$. Red dashed-line: arrival of leading-edge diffraction (rigid plate), green dashed-line: arrival of trailing-edge diffraction (rigid plate), blue dashed-line: band-adaptive time-window.

3.3. Diffraction-Locked Band Analysis

The processed scattered IRs were analysed using an event-locked, frequency-adaptive windowing procedure. For each grazing angle, the Hann analysis window was centred on the diffraction peak detected in the rigid reference measurements at every receiver position.

For each one-third-octave band, the window length was chosen to contain 1.5 oscillation cycles at the corresponding centre frequency. The windowed responses were transformed to the frequency domain, where the one-third-octave-band amplitudes were extracted after applying a bounded frequency-dependent correction derived from the free-field deconvolution reference to compensate for amplitude changes introduced by the regularised deconvolution. The corrected band amplitudes were subsequently normalised using the median free-field band amplitude over a fixed microphone patch to compensate for angle-dependent source-distance variations. Receiver positions within the specular region were excluded from the analysis. The resulting band amplitudes, denoted by $A_b(x, z)$, were used to generate spatial diffraction-induced level maps. Finally, for each frequency band b, the aperture-integrated diffraction-induced energy was computed as

$$E_b = \sum_{(x,z)\in\Omega_{\text{diff}}} A_b^2(x, z), \tag{4}$$

where Ω_{diff} denotes the set of receiver positions within the diffraction region. The corresponding integrated level relative to the rigid reference was then obtained as

$$L_{\text{diff},b} = 10 \log_{10} \left(\frac{E_b}{E_{b,\text{rigid}}} \right), \tag{5}$$

where $E_{b,\text{rigid}}$ denotes the corresponding integrated energy of the rigid reference for the same grazing angle.

4. Results

4.1. Normalized Spatial Levels

Figure 3 presents the diffraction-induced level distribution in the 500, 1600, and 3150 Hz one-third-octave bands. Within each band, the rigid plate, bioboard, and rigid-backed bioboard are shown at grazing angles of 0°, 8°, 21°, and 31°. Each band is normalized by a common maximum across all displayed materials and grazing angles. The arrow indicates the propagation direction toward the leading edge.

At 500 Hz, all three materials exhibit smooth spatial distributions with only moderate material-dependent differences. Increasing the grazing angle produces progressively higher diffraction-induced levels near the leading edge and farther downstream, while the spatial variation remains comparatively gradual.

At 1600 Hz, the spatial gradients become sharper and the differences between the rigid and porous configurations become more evident. Relative to the rigid plate, porous configurations exhibit broader low-level regions,

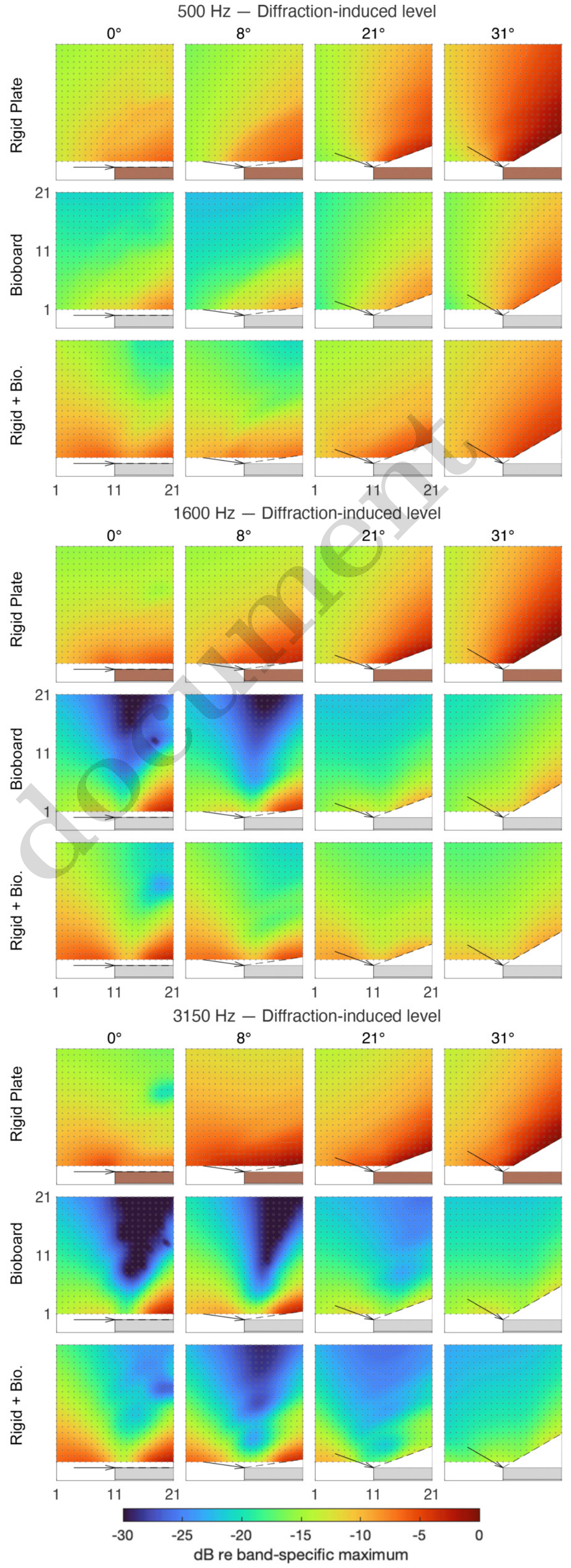

Figure 3: Diffraction-induced levels normalized to the per-band maximum. Arrows pointed to the leading edge indicate propagation direction. Material thicknesses are shown schematically and are not to scale.

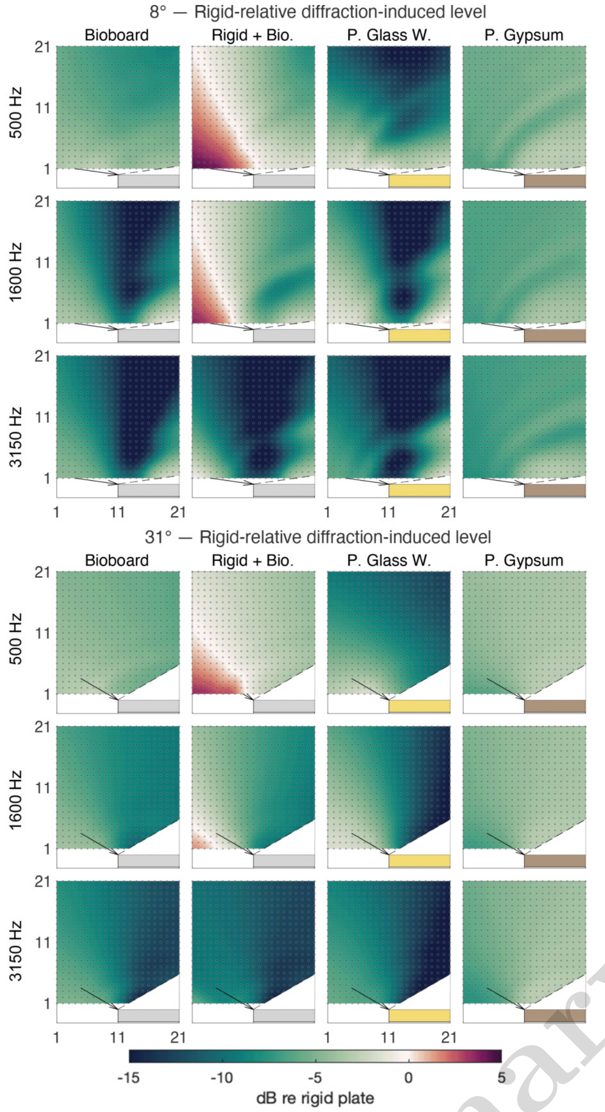

Figure 4: Diffraction-induced level relative to the rigid reference for grazing incidence at (a) 8° and (b) 31°. Material thicknesses are shown schematically and are not to scale.

particularly at the shallower grazing angles. The rigid backing also modifies the upstream and near-edge level distribution relative to the unbacked bioboard. At the shallower grazing angles, the increased levels over the porous surface may indicate contributions potentially associated with surface-wave phenomena. At 3150 Hz, the material-dependent differences are most pronounced. Both porous configurations exhibit strongly localized low-level regions above and downstream of the leading edge, in contrast to the generally smoother and higher-level distribution produced by the rigid plate. The spatial extent and location of these regions vary systematically with grazing angle. Overall, the rigid plate produces a smooth fan-shaped diffraction pattern, whereas the porous configurations exhibit increasingly localized and material-dependent level distributions with increasing frequency.

4.2. Rigid-Relative Spatial Levels

Figure 4 shows the diffraction-induced levels relative to the rigid reference for grazing angles of 8° and 31°. With the exception of the rigid-backed bioboard, all materials predominantly exhibit negative levels, indicating lower diffraction-induced levels than the rigid plate. The attenuation becomes increasingly pronounced with frequency for the bioboard and perforated glass-wool samples, whereas the perforated gypsum exhibits relatively small deviations from the rigid reference over the investigated frequency range. The rigid-backed bioboard, and to a lesser extent the perforated glass-wool at 8°, localized amplification relative to the rigid reference, particularly upstream of the leading edge and at low-to-mid frequencies. At 8°, a pronounced attenuation valley develops above the leading edge for all porous materials except in the 500 Hz band.

Increasing the grazing angle from 8° to 31° generally reduces the spatial variability for all materials, resulting in more uniform attenuation relative to the rigid reference.

4.3. Aperture-Integrated Energy Levels

Figure 5 shows the aperture-integrated diffraction-induced energy levels relative to the rigid reference for the bioboard and rigid-backed bioboard as a function of frequency and grazing angle. The bioboard consistently provides greater attenuation than the rigid-backed bioboard, particularly below approximately 2 kHz. At shallow grazing angles (8° and below), this behaviour extends across the entire investigated frequency range, whereas the rigid-backed bioboard exhibits diffraction-induced energy levels comparable to those of the rigid reference over much of the frequency range below 2 kHz.

The rigid-backed bioboard follows a similar overall frequency dependence but consistently exhibits weaker attenuation than the bioboard. In both configurations, the attenuation generally increases with increasing frequency and grazing angle, although the frequency dependence is less pronounced at the shallower grazing angles. Note that transmission effects are expected

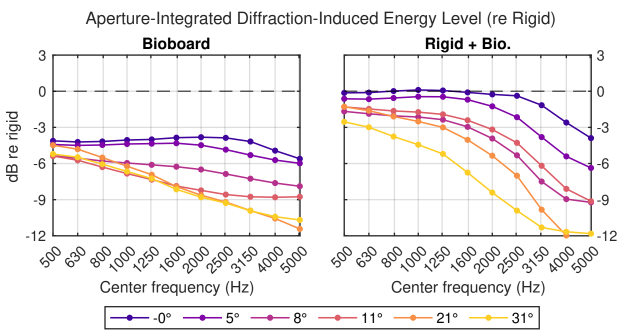

Figure 5: Aperture-integrated diffraction-induced energy level relative to the rigid reference for bioboard (3 cm) and rigid plate (2 cm) + bioboard (3 cm), shown as a function of 1/3-octave center frequency for multiple grazing angles.

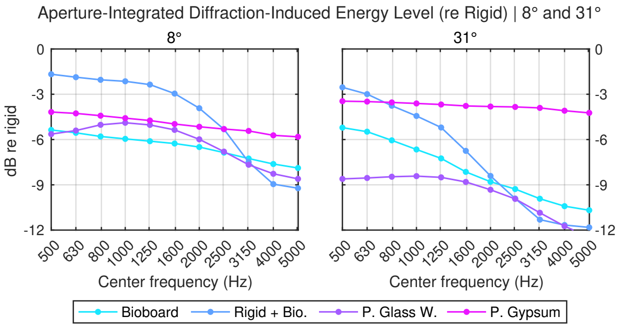

Figure 6: Aperture-integrated diffraction-induced energy level relative to the rigid reference for different samples and grazing angles, shown as a function of 1/3-octave center frequency.

only in the bioboard (non-rigid-backed) configuration. Figure 6 shows the aperture-integrated diffraction-induced energy levels relative to the rigid reference for grazing angles of 8° and 31°. At 8°, the bioboard, perforated glass wool, and perforated gypsum exhibit broadly similar attenuation levels over much of the investigated frequency range, whereas the rigid-backed bioboard exhibits markedly higher diffraction-induced energy levels below approximately 2.5 kHz. In contrast to the other materials, the perforated gypsum exhibits nearly frequency-independent attenuation at both grazing angles. At 31°, it shows only slightly weaker attenuation than at 8°, whereas the attenuation increases for the bioboard, rigid-backed bioboard, and particularly the perforated glass wool.

5. Conclusions

An experimental framework based on dense planar measurements was presented to investigate leading-edge diffraction under grazing incidence for finite-sized rigid, porous, and perforated samples. By combining free-field subtraction with event-locked, frequency-adaptive time windows, diffraction-induced sound fields were consistently characterised and compared across materials, frequencies, and grazing angles.

The rigid reference exhibited a smooth fan-shaped diffraction pattern at low and mid frequencies, while porous and perforated materials generally reduced the diffraction-induced levels relative to the rigid reference. The magnitude and spatial distribution of this attenuation depended on material type, backing condition, frequency, and grazing angle. The rigid-backed bioboard exhibited localized amplification at low frequencies and shallow grazing angles, whereas the perforated gypsum board remained comparatively insensitive to frequency and grazing angle. At shallow grazing angles, a vertically elongated attenuation region developed above the leading edge of the porous materials and became increasingly pronounced at mid-to-high frequencies. At larger grazing angles, the porous samples exhibited progressively stronger attenuation towards the specular boundary.

The proposed methodology provides a framework for the quantitative characterization of edge-related scattering from finite absorbers and enables systematic comparison of diffraction-induced sound fields across different materials and grazing-incidence conditions.

References

[1] M. A. Biot and I. Tolstoy, "Formulation of wave propagation in infinite media by normal coordinates with an application to diffraction," *The Journal of the Acoustical Society of America*, vol. 29, no. 3, pp. 381–391, 1957.

[2] H. Medwin, "Shadowing by finite noise barriers," *The Journal of the Acoustical Society of America*, vol. 69, no. 4, pp. 1060–1064, 1981.

[3] U. P. Svensson, R. I. Fred, and J. Vanderkooy, "An analytic secondary source model of edge diffraction impulse responses," *The Journal of the Acoustical Society of America*, vol. 106, no. 5, pp. 2331–2344, 1999.

[4] D. Chu, T. K. Stanton, and A. D. Pierce, "Higher-order acoustic diffraction by edges of finite thickness," *The Journal of the Acoustical Society of America*, vol. 122, no. 6, pp. 3177–3194, 2007.

[5] M. J. Priddin, C. C. Paruchuri, P. Joseph, and L. J. Ayton, "A semi-analytic and experimental study of porous leading edges," in *25th AIAA/CEAS Aeroacoustics Conference*, 2019, p. 2552.

[6] X. Huang, H. Zou, and X. Qiu, "Effects of the top edge impedance on sound barrier diffraction," *Applied Sciences*, vol. 10, no. 17, p. 6042, 2020.

[7] L. Yang, S. Zhao, and B. Halkon, "An efficient algorithm to calculate the diffracted sound field by a sound-absorbing barrier on an impedance ground," *The Journal of the Acoustical Society of America*, vol. 159, no. 6, pp. 5541–5553, 2026.

[8] U. P. Svensson, V. Henriksen, and H. Olsen, "Handling impedance surfaces in diffraction modeling," *Acta Acustica*, vol. 9, p. 23, 2025.

[9] M. Ottink, J. Brunskog, C.-H. Jeong, E. Fernandez-Grande, P. Trojgaard, and E. Tiana-Roig, "In situ measurements of the oblique incidence sound absorption coefficient for finite sized absorbers," *The Journal of the Acoustical Society of America*, vol. 139, no. 1, pp. 41–52, 2016.

[10] M. Yuzawa, "A method of obtaining the oblique incident sound absorption coefficient through an on-the-spot measurement," *Applied Acoustics*, vol. 8, no. 1, pp. 27–41, 1975.

[11] E. Mommertz, "Angle-dependent in-situ measurements of reflection coefficients using a subtraction technique," *Applied Acoustics*, vol. 46, no. 3, pp. 251–263, 1995.